DON'T MISS OUR SPECIAL SESSION AT ASTRO

Performing QA Remotely in the Age of COVID

October 26, 11:45 AM EST

At home. On site. **In sync.**

SunCHECK™ enables complete, collaborative **remote QA coverage** for COVID-19 & beyond.

Click to explore:

- Advantages of a centralized Patient & Machine QA solution
- How SunCHECK eased the transition to remote work for users worldwide
- Three new ways we're simplifying Platform adoption

Go to: **sunnuclear.com/getprepared**

SUN NUCLEAR corporation

Patient Safety Starts Here

Tumor phase recognition using cone-beam computed tomography projections and external surrogate information

Pingfang Tsai, Guanghua Yan, and Chihray Liu
Department of Radiation Oncology, College of Medicine, University of Florida, Gainesville, Fl 32610-0385, USA

Ying-Chao Hung
Department of Statistics, National Chengchi University, Taipei 11604, Taiwan

Darren L. Kahler, Ji-Yeon Park, Nick Potter, Jonathan G. Li, and Bo Lu[a)]
Department of Radiation Oncology, College of Medicine, University of Florida, Gainesville, Fl 32610-0385, USA

(Received 15 January 2020; revised 10 May 2020; accepted for publication 18 May 2020; published xx xxxx xxxx)

Purpose: Directly extracting the respiratory phase pattern of the tumor using cone-beam computed tomography (CBCT) projections is challenging due to the poor tumor visibility caused by the obstruction of multiple anatomic structures on the beam's eye view. Predicting tumor phase information using external surrogate also has intrinsic difficulties as the phase patterns between surrogates and tumors are not necessary to be congruent. In this work, we developed an algorithm to accurately recover the primary oscillation components of tumor motion using the combined information from both CBCT projections and external surrogates.

Methods: The algorithm involved two steps. First, a preliminary tumor phase pattern was acquired by applying local principal component analysis (LPCA) on the cropped Amsterdam Shroud (AS) images. In this step, only the cropped image of the tumor region was used to extract the tumor phase pattern in order to minimize the impact of pattern recognition from other anatomic structures. Second, by performing multivariate singular spectrum analysis (MSSA) on the combined information containing both external surrogate signal and the original waveform acquired in the first step, the primary component of the tumor phase oscillation was recovered. For the phantom study, a QUASAR respiratory motion phantom with a removable tumor-simulator insert was employed to acquire CBCT projection images. A comparison between LPCA only and our method was assessed by power spectrum analysis. Also, the motion pattern was simulated under the phase shift or various amplitude conditions to examine the robustness of our method. Finally, anatomic obstruction scenarios were simulated by attaching a heart model, PVC tubes, and RANDO® phantom slabs to the phantom, respectively. Each scenario was tested with five real-patient breathing patterns to mimic real clinical situations. For the patient study, eight patients with various tumor locations were selected. The performance of our method was then evaluated by comparing the reference waveform with the extracted signal for overall phase discrepancy, expiration phase discrepancy, peak, and valley accuracy.

Results: In tests of phase shifts and amplitude variations, the overall peak and valley accuracy was -0.009 ± 0.18 sec, and no time delay was found compared to the reference. In anatomical obstruction tests, the extracted signal had 1.6 ± 1.2 % expiration phase discrepancy, -0.12 ± 0.28 sec peak accuracy, and 0.01 ± 0.15 sec valley accuracy. For patient studies, the extracted signal using our method had -1.05 ± 3.0 % overall phase discrepancy, -1.55 ± 1.45% expiration phase discrepancy, 0.04 ± 0.13 sec peak accuracy, and -0.01 ± 0.15 sec valley accuracy, compared to the reference waveforms.

Conclusions: An innovative method capable of accurately recognizing tumor phase information was developed. With the aid of extra information from the external surrogate, an improvement in prediction accuracy, as compared with traditional statistical methods, was obtained. It enables us to employ it as the ground truth for 4D-CBCT reconstruction, gating treatment, and other clinic implementations that require accurate tumor phase information. [https://doi.org/10.1002/mp.14298]

Key words: lung, tumor phase recognition, principal component analysis, singular spectrum analysis, gating

1. INTRODUCTION

Radiation therapy requires precise dose delivery to the intended treatment region. Accurate treatment delivery to lung cancers is particularly challenging as the tumor is continuously moving along with the respiratory cycles during the treatment. Respiratory-induced tumor motion is one of the potential sources of error in lung radiation therapy. Many

motion management approaches[1,2] have been developed to improve the delivery accuracy to the lung tumors. Respiratory gating[3] is one of these. Respiratory gating controls the radiation beam on/off status depending on whether the tumor is inside or outside the treatment fields during the treatment. It often uses either external or internal surrogates to trigger the beam.[4–7] However, respiratory phase inconsistency between the tumor and surrogates is not uncommon and largely depends on the tumor location and patient respiratory pattern.[8–11] Thus, the ability to accurately extract the phase correlation between the tumor and surrogates becomes crucial to ensure accurate gating-based delivery. Four-dimensional cone-beam computed tomography (4D-CBCT) is another contemporary technique for respiratory motion management. As 4D-CBCT images include both spatial and temporal information of tumor and surrounding anatomy, they allow the clinician to determine the tumor motion range and make subsequently clinical decisions with regard to tumor alignment. Tumor phase information also plays a crucial role in the imaging reconstruction process of 4D-CBCT. Correct phase sorting can largely reduce the motion artifact of the reconstructed images of each phase.

Directly tracing lung tumor movement and extracting the phase information has traditionally been a difficult task, primarily due to the inability of acceptable tumor-soft tissue distinction using traditional image modalities for tumor tracking (e.g., kilovoltage (KV) x-ray images, megavoltage (MV) x-ray images, CBCT images, ultrasound images, etc.). Magnetic resonance-guided radiation therapy (MRgRT) provides the potential to extract tumor motion since it provides a decent contrast between the tumor and surrounding tissues.[12] However, due to the high cost and limited production, the use of MRgRT is still limited, and the use of it for tumor tracking is still in the research stage.[13] An alternative strategy for tumor phase extraction is to extract tumor phase information using surrogate information *in lieu of* the tumor itself. Two major methodologies using such a strategy have been widely developed and applied. One uses external surrogate information to extract the phase information, whereas the other uses internal surrogate information. The former has become much more popular than the latter for recent clinical applications, as most of the external surrogate information can be easily acquired by readily available detection devices such as pressure sensors and infrared cameras, etc. Typical external surrogate acquisition system includes the bellow system (Phillips Healthcare, Cleveland, OH, USA), real-time position management (RPM) system (Varian Medical Systems, Palo Alto, CA, USA), AlignRT® system (Vision RT, London, England). The information extracted by those systems contains the distinct oscillation of respiratory cycles. However, the extracted information possesses an intrinsic discrepancy with the real tumor motion since the phase between external surrogates and internal tumor or anatomical structures is not necessarily congruent.[8–10] Internal surrogate-based methods can potentially overcome such drawbacks. Ideally, if the surrogate is proximal or even inside the tumor, the detected phase information can be treated as the phase information of the tumor. Such attempts have been made by implanting fiducial markers[14–17] or electromagnetic transponder beacons[18–20] into the tumor region and then using x-ray image modalities or radiofrequency methods to track them. However, the implanting procedures are invasive, which can cause the risk of pneumothorax[21,22] or pulmonary hemorrhage.[23] Moreover, the implanted surrogate may experience migration throughout the treatment.[24,25]

Considering the practicality and risks of marker implantation methods, clinicians and researchers have developed alternative methods to reconstruct the tumor waveform using projected KV images. Many researchers have attempted to recover the internal respiratory phase information using CBCT projections. The strategies include intensity-based methods such as the Amsterdam Shroud (AS) method,[26] the intensity analysis (IA) method[27]; frequency domain methods, such as the Fourier transform method (FT)[28]; and statistical-based methods such as the local principal component analysis (LPCA) algorithm[9] and a two-step L1-norm LPCA method.[10] All of these methods can effectively recover the phase information using the identifiable surrogate information. The LPCA statistical method is more robust than intensity-based methods in general.[9] It not only uncovers the underlying structure of the dataset, but also provides the flexibility of choosing the principal components and, at the same time, discards sources of noise and outliers. Nevertheless, the limitations of these methods are significant. First, due to the weakness of tumor phase information in the original projections, surrogates with strong and distinct signals (e.g., diaphragm) have to be included in order to enhance the reconstructed signals. However, this process would only extract internal-surrogate-like information rather than the true tumor phase information. The discrepancies largely depend on the relative anatomical location of the tumor with respect to the surrogate, as well as respiratory physiology. Additionally, missing surrogate information from the images due to poor contrast, anatomical obstruction, or imaging cutout can also undermine the quality of the phase signal reconstruction with these approaches.

In this study, we proposed a robust statistical method to overcome the disadvantage of current surrogate methods by utilizing both external surrogate and CBCT projection images. With the assistance of external motion information, this method is able to improve the phase information extraction accuracy, as compared with traditional statistical methods. A validation experiment using phantom and patient data was also assessed and the results are presented.

2. MATERIALS AND METHODS

Prior to the detailed description of our method, an algorithm outline was given here for the sake of clarity. First, the tumor-only region of each projection was cropped to generate the AS image. Second, the LPCA method was used to extract the initial respiratory waveform signal from the AS image. Third, the surface motion (used as the external surrogate) was acquired by recording the movement of an infrared marker on the patient or the phantom. Finally, the multivariate singular

spectrum analysis (MSSA) method was applied to recover the tumor's respiratory cycles in a waveform format by combining the oscillatory information from both the external surrogate and the internal structures.

In the following section, equipment and methodologies used for projections and external signal acquisitions were first introduced. A phase reconstruction algorithm using acquired signals was then described systematically. The evaluation methods tested on both phantoms and patients were depicted in the end.

2.A. Raw data acquisition of CBCT projections and external signals

2.A.1. Acquisition of the projections using CBCT

3D-CBCT projections were used as the raw data to reconstruct the initial internal signal. An Elekta Versa HD^{TM} linac accelerator (Elekta Inc., Stockholm, Sweden) with an x-ray volume imaging (XVI) system was utilized for CBCT scan. As shown in Fig. 1(a), XVI system consists of a kilovoltage (KV) x-ray source and a KV flat panel detector mounted on the linac gantry. A typical 360-degree acquisition for a full CBCT scan took about 2 min to accomplish and produces around 700 projection images. Each projection image with 512 × 512 pixels was acquired by a KV image receptor with a 0.8 mm pixel size. The sampling rate was around 0.183 sec per projection.

2.A.2. Acquisition of the external signal using the Optical Tracking System (OTS)

The external surrogate for the test objects was an infrared marker attached to the surface of the test object (either phantoms or patients) and its real-time position was captured by the optical tracking system (OTS) with a pair of infrared cameras mounted on the room ceiling, as shown in Fig. 1(b). For phantoms, the infrared reflective marker was attached to the outside of the phantom's movable insert, as shown in [Fig. 1(a) and 1(c)]; for patients, an infrared reflective (IR) marker was placed on the skin surface of the abdominal region approximately 5 cm inferior to the xiphoid process at the midline of the patient.

2.A.3. Synchronization between internal and external data

The acquisition of the temporal correlation between internal and external data is essential for signal reconstruction. An additional reflective marker was attached to the KV flat panel to setup such a correlation, shown in [Fig. 1(a)]. Since the relationship between the gantry angle and the KV panel marker position can be empirically determined, the correspondence between the gantry angle of projection acquisition and the surface marker position during the scan can be indirectly established by simultaneously tracing the KV panel marker and the surface external surrogate marker. By mining the CBCT acquisition log file, one-to-one correspondence between the projection and its acquired gantry angle was extracted. Accordingly, the final correlation between the acquired projection images and their corresponding surface marker positions during the scan was ultimately determined.

2.B. Tumor phase reconstruction algorithm using external signal and CBCT projections

2.B.1. Amsterdam Shroud (AS) image generation using CBCT projections

In this work, an AS image of the CBCT projection was used as the initial input signal for tumor phase reconstruction.

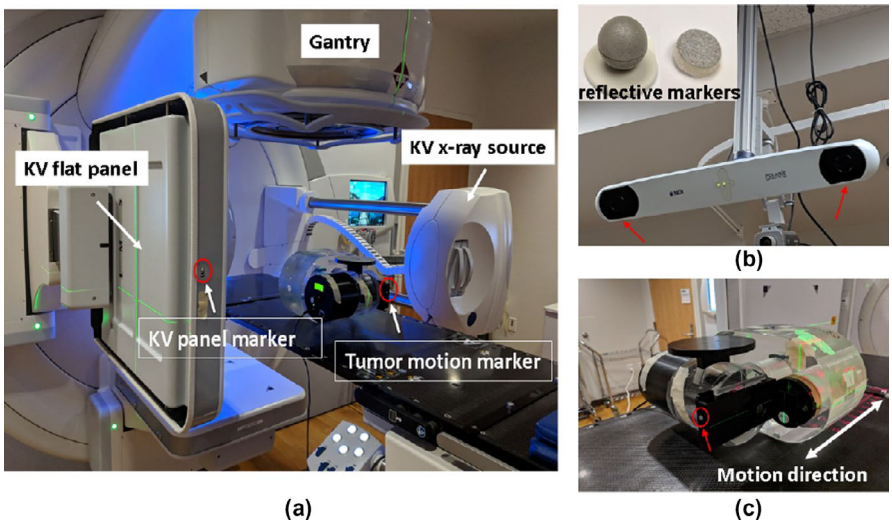

FIG. 1. The experiment design for the study. (a) The cone-beam computed tomography (CBCT) system with KV x-ray source and KV flat panel detector are shown. Infrared reflective markers were attached to the side of KV flat panel and to the movable insert of the phantom. (b) The optical tracking system (OTS) is equipped with two infrared cameras to capture the real-time positions of the reflective markers. (c) The motion direction of the QUASAR^{TM} respiratory motion phantom is indicated by the white arrow. The circle indicates the location of the attached infrared reflective marker. Its real-time location was used as the ground truth for the phantom study.

The construction method of AS images (taken from selected literature[9,10]) that was applied in our study is described as follows. First, each projection image was initially converted to the inversed intensity image and further converted to the attenuation image by taking the logarithm of the intensity image. This process is able to improve the image contrast and tumor visibility. Second, the cranial-caudal (CC) derivative image was generated from the attenuation image in order to enhance the anatomic features of the image. Third, the derivative images of the tumor region with 5 mm margins were cropped for column array generation. Fourth, an initial AS image was formed by affixing all the column arrays together (in the order of projection image received) into a 2D matrix. Last, to improve the homogeneity of the AS images, the initial AS image was reprocessed to generate the final AS image by applying the adaptive z-normalization method suggested by Chao et al.[10] The detailed steps of the adaptive z-normalization process are described in the work of Chao et al.[10] and will not be repeated here. The overall workflow is illustrated in Fig. 2 for a better understanding.

The distinction between our method and other methods[9,10] is the region-of-interest (ROI) selection for column array generation. Unlike other methods that use the whole projection images, we only employed the cropped ROI in the tumor region. The rationale behind this was to minimize the impact of the signal interference from surrounding anatomic structures (e.g., diaphragm) and/or nonhuman tissue artifacts (e.g., pacemaker, implants, or treatment couch top). The size and location of the region-of-interested (ROI) were determined by the patient's tumor location, tumor size, and tumor motion range estimated from the four-dimensional computed tomography (4D-CT) scans. The central location of the ROI on the projection image was defined as the projection point for the centroid of the internal tumor volume (ITV) on the projection images. The ROI is shown as the rectangle shape in Fig. 2, which covers the ITV projection on the CBCT projection images with a 5 mm expansion on each side.

2.B.2. Initial respiratory waveform extraction using Local Principal Component Analysis (LPCA)

Once the tumor-AS image was obtained, it was then used as the input signal for the initial phase signal extraction using the LPCA method. The LPCA method can effectively reconstruct the waveform for the cases presented in the original paper.[9] However, its accuracy can be affected by the pixel intensity of the surrounding structures, especially the diaphragm. LPCA also performed poorly when the tumor was obstructed by multiple anatomical structures, which takes place frequently in the clinical environment. Nevertheless, it does provide a reasonable starting point to generate the initial waveform. Figure 3 shows the basic workflow of the algorithm, which can be briefly depicted as follows.

First, a LPCA window width, W, is selected, and the window moves sequentially by one column along the horizontal direction on the tumor-AS image. In the first window, the eigenvectors associated with the first PC are selected for the principal direction since they reflect the most significant variance in the data, and the PC scores are used as the extracted signal for columns 1 to [W/2]+1. To ensure the continuity of the extracted curve for the following windows, the correlation of each of the first five PCs with the PC obtained from the

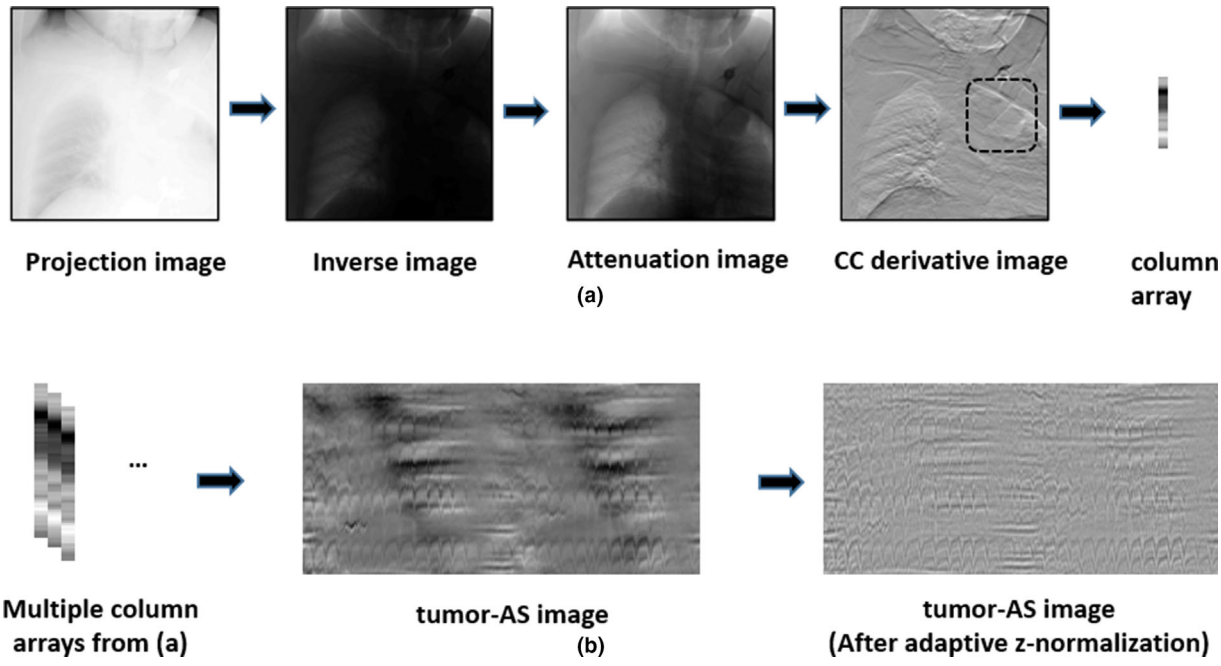

FIG. 2. Tumor-Amsterdam Shroud (AS) image generation. (a) The image processing steps from the original projection image to a column array where only the pixel values within the tumor region-of-interest were summed. (b) The initial AS image was generated by assembling each column array in the order of each projection that was received to form a tumor-AS image and the final AS image after applying adaptive z-normalization.

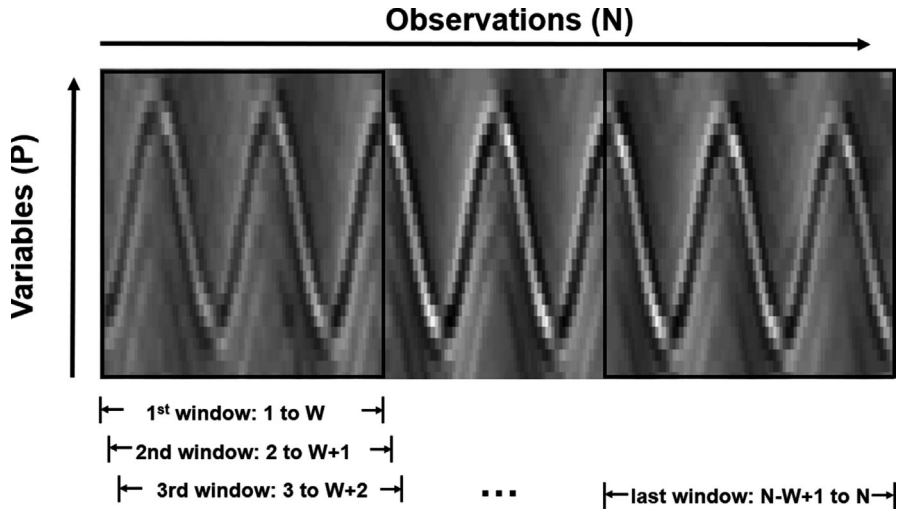

FIG. 3. Local principal component analysis (LPCA) application on the Tumor-Amsterdam Shroud image. Note that N is the total number of projections, W is the LPCA window width, and P is the variable that depends on the selected tumor ROI size. W is the window width while performing LPCA and the number of observations is equal to W, in for the case shown.

previous window is calculated. Subsequently, the PC with the highest correlation is selected as the principal direction for the current step. The corresponding PC score for the center column is selected as the extracted signal for this column. To keep the principal direction consistent with the one obtained from the previous step, a sign reversal may be necessary (since the PCA cannot distinguish between the positive and negative direction). In this study, the directional information was fed in from the real-time external surrogate signal by the OTS. This process was repeated until the last window, from N-W + 1 to N, was reached. In this study, we chose W from one to three breathing cycles, as suggested by Yan et al.[9]

2.B.3. Final respiratory waveform reconstruction using external surrogate information

On one hand, the initial respiratory waveform obtained using LPCA could potentially present some inconsistent and perturbed patterns, especially for the observation window formed by the lateral projection views. On the other hand, unlike internal signals, this phenomenon is not presented in the external surrogate signal since no obstruction is presented between the surrogate (fiducial marker) and the detection system (infrared camera). Thus, if we can utilize the external signal to enhance the perturbed signals of the initial waveform, the unperturbed internal signal can conceivably be reconstructed. Following this concept, a statistic method, called multivariate singular spectrum analysis (MSSA), was introduced in this study to achieve this goal. The algorithm details are provided as follows:

First, let us define the initial respiratory waveform acquired using LPCA as a one-dimensional time series denoted by $\mathbf{X} = \{x_t : t \in 1, \ldots, N\}$, where t represents the observation of the time series from 1 to N with an equal time interval (gantry angle interval between projections); x_t represents the magnitude at t. Then, a trajectory matrix, $\mathbf{Y}$, is created by stacking X_i from $i = 1$ to K, which possesses M consecutive observations and offset starting elements, as indicated in Eq. (1). M is an embedding time-delayed dimension, typically, 1 to 3 breathing cycles, and $K = N - M + 1$.

$$\mathbf{Y} = \begin{bmatrix} X_1 \\ X_2 \\ X_3 \\ \vdots \\ X_k \end{bmatrix} = \begin{bmatrix} x_1 & x_2 & x_3 & \cdots & x_M \\ x_2 & x_3 & x_4 & \cdots & x_{M+1} \\ x_3 & x_4 & x_5 & \cdots & x_{M+2} \\ \vdots & \vdots & \vdots & \ddots & \vdots \\ x_K & x_{K+1} & x_{K+2} & \cdots & x_N \end{bmatrix}. \quad (1)$$

The structure of matrix $\mathbf{Y}$ innately correlates the underlying oscillation respiratory pattern as the time evolved. It allows us to capture the signature of the dynamic behavior of the respiratory waveform in a much easier way than does the original time-series format.

Applying the same method, we can construct a time series and its corresponding trajectory matrix for the external surrogate signal as well. Now, two channels of time series are created in our study: Channel 1 is the external surrogate signal from OTS denoted by $\boldsymbol{X}1(\boldsymbol{t})$; channel 2 is the preliminary result from LPCA step denoted by $\mathbf{X2}(t)$. $\mathbf{Y1}$ and $\mathbf{Y2}$ are the corresponding trajectory matrix, respectively. Now, a grand covariance matrix between the two time series can be formed using Eq. (2), as illustrated in Fig. 4.

$$\mathrm{C} = \mathbb{Y}'\mathbb{Y}(N - M + 1) \text{ as } \mathbb{Y} = [\mathbf{Y1}, \mathbf{Y2}] \quad (2)$$

where $(\cdot)'$ indicates the transpose of a matrix.

Matrix $\mathbf{C}$ represents the covariance between X_t and $X_{t+\tau}$ with time lag of $\tau = 0, \ldots, M - 1$. It includes auto- and cross-covariance from both of the time series, X1(t) and X2(t). More specifically, four-quadrant submatrix of $\mathbf{C}$: C(1,1), C(1,2), C(2,1), and C(2,2) represent the covariance between the neighbor observations of X1 (t) and itself, X1 (t) and its X2 (t) counterpart, and X2 (t) and its X1 (t) counterpart, and X2 (t) and itself, respectively.

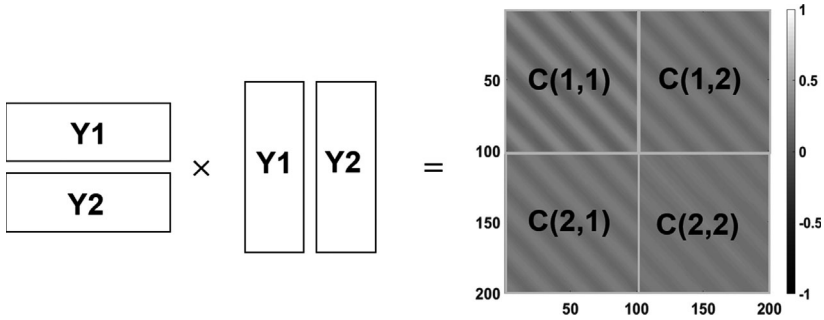

FIG. 4. The grand block structure of covariance **C**. **Y1** and **Y2** are the trajectory matrix of time series $X1(t)$ and time series $X2(t)$, respectively.

With this mathematical arrangement, the correlation of each data point was established. The establishment was not limited to the neighboring data points in the same time series; it also included the correlation between corresponding points from both time series.

Second, the eigenvalues and eigenvectors of **C** are obtained by performing singular value decomposition (SVD). Since **C** is a symmetric and positive semi-definite matrix, let us denote its ordered eigenvalues by $\lambda_1 \geq \lambda_2 \geq \ldots \geq \lambda_d \geq 0$ and the corresponding orthogonal eigenvectors by $e_1, e_2, \ldots, e_d$. Let $D = \max\{i : \lambda_i > 0\}$(i.e., the number of eigenvalues) and the matrix for eigenvectors (**V**) is:

$$\mathbf{V} = [e_1 : \ldots : e_D] = \begin{bmatrix} v_{1,1} & v_{2,1} & \cdots & v_{D,1} \\ v_{1,2} & v_{2,2} & \cdots & v_{D,2} \\ v_{1,3} & v_{2,3} & \cdots & v_{D,3} \\ \vdots & \vdots & \ddots & \vdots \\ v_{1,2M} & v_{2,2M} & \cdots & v_{D,2M} \end{bmatrix}. \quad (3)$$

Once the orthogonal eigenvectors were obtained, the principal component (**PC**) can be calculated by projecting the data, $\mathbb{Y}$, onto linearly uncorrelated orthogonal axes in the principal component space. This is a grouping step where it is disjointed into D subsets. Thus, each principal component can be calculated using Eq. (4)

$$\mathbf{PC}_j = \mathbb{Y}e_j (j = 1, \ldots, D). \quad (4)$$

To reconstruct the trajectory matrix, $\mathbb{Y}^{(r)}$, possessing only the most dominant PCs, an invert projection method is used as shown in Eq. (5) and (6). Each PC, $\mathbf{PC}_j$ is projected back to the original data-centric coordinates. It yields $\mathbb{Y}_j$ as follows:

$$\mathbb{Y}_j = \left[\mathrm{Y1}_j, \mathrm{Y2}_j\right] = \mathrm{PC}_j e_j' = \mathbb{Y}e_j e_j'. \quad (5)$$

Then, the linear combination of the invert projected principal component yields the best approximation of $\mathbb{Y}$ as $\left\|\mathbb{Y} - \mathbb{Y}^{(r)}\right\|$ is the minimum.

$$\mathbb{Y}^{(r)} = \left[\mathbb{Y}1^{(r)}, \mathbb{Y}2^{(r)}\right] = \sum_{j=1}^{\mathrm{m}} \mathbb{Y}_j = \sum_{j=1}^{m} \left[\mathbf{Y}1_j, \mathbf{Y}2_j\right] \quad (6)$$

where $\boldsymbol{m}$ ($\boldsymbol{m} \leq D$) represents the index of the first $\boldsymbol{m}$ number of the most dominant PCs.

The selection of $\boldsymbol{m}$ is based on the weight of each PC. It required the summation of its corresponding eigenvalue, normalized to the summation of the total eigenvalues, be greater than a threshold, T, ranging from 0.9 to 0.98 (manually chosen for each case in our study). This can be expressed mathematically as:

$$\min\left\{m : \frac{\sum_{i=1}^{m} \lambda_i}{\sum_{j=1}^{D} \lambda_j} \geq T\right\}. \quad (7)$$

Lastly, we reconstruct internal tumor waveform, $\mathbf{X}2^{(r)}$, from $\mathbb{Y}2^{(r)}$ using the Hankelization procedure. The detailed procedure will not be repeated here. The interested reader can refer to Golyandina et al.[29]

2.C. Algorithm evaluation using phantom and patient data

2.C.1. Phantom study

A QUASAR™ 4D respiratory motion phantom (Modus Medical Devices Inc., London, Canada) was employed for respiratory simulations. The signal received from the IR marker on the movable insert was used as the ground truth; the extracted tumor motion signal from the CBCT projection images is utilized for the reconstructed waveform. Our method consisted of four parts: (a) The reconstructed results between the LPCA and our LPCA–MSSA method were compared in the frequency domain using power spectrum analysis for a sinusoidal respiratory motion case. (b) The sensitivity of the CBCT scanning uncertainty was tested for the respiratory waveforms reconstructed by both the LPCA–MSSA and the LPCA method using 10 repeated CBCT scans. Peak-Valley time differences and phase discrepancy from the ground truth among repeated scans were analyzed. (c) The robustness test of the LPCA–MSSA method on the phase shift and amplitude variation of the external surrogate was performed as well. Three arbitrary phase shifts and three amplitude variations were altered from the original external surrogate signal (a 12 breath-per-minute (BPM) sinusoidal waveform) with multiple sine functions and weightings for testing purposes. (d) Lastly, the influence of anatomical structure obstructions on the waveform reconstruction was assessed. Three

anatomical obstruction scenarios were simulated. The first scenario simulated obstruction by the heart using a solid-filled three-dimensional (3D)-printed heart placed at the side of the phantom. The second scenario simulated rib obstruction by placing polyvinyl chloride (PVC) tubes on the top and two sides of the phantom in a parallel arrangement. The third scenario simulated multiple tissue perturbations in the lung region with Rando® phantom slabs placed around the QUASAR^{TM} 4D phantom. Figure 5 demonstrates the placement of the various simulated structures. Five respiratory patterns, including sinusoidal, cardiac artifact, jitter artifact, triangular, and typical fast breathing waveform, were applied for each obstruction scenario to ensure the versatility of the method. The extracted results were then compared to the ground truth.

2.C.2. Patient study

Eight patient cases with various tumor sizes (range from 2.8 c.c. to 63.2 c.c.) and locations inside the lungs [demonstrated in Fig. 6(a)] were investigated in this study. Two of them have artificial implants of high-density materials proximate to the lung areas, which are shown on the CBCT projection images of [Fig. 6(b)]. The tumor size varies from 1.5 to 5.5 cm, and the tumor motion range is from 3.5 to 20 mm. Unlike the phantom study, for which internal tumor motion can be accurately simulated and confirmed, the actual tumor motions of patients are unknown. However, a reference tumor motion waveform can still be extracted by tracing the tumor position on the projection images using the following procedure. First, the window and level of each projection image are manually adjusted in order to obtain the best visibility of the tumor on each projection. Second, the most superior and inferior extent of the tumor on each projection was identified by a radiation oncologist and subsequently projected onto the tumor-AS image. Third, the corresponding tumor center position was obtained by averaging the corresponding superior and inferior extents. Finally, the reference waveform of the center of the tumor was established by tracing the corresponding center locations on the tumor-AS image.

The congruency between the reference waveform and the extracted waveform was examined with respect to overall phase discrepancy, expiration phase discrepancy, peak accuracy, and valley accuracy. In addition, the percentage of variance and the number of PCs required were also assessed.

3. RESULTS

3.A. Phantom study

The power spectrum density (PSD) generated by the ground truth waveforms and the waveforms reconstructed by the LPCA method and the LPCA–MSSA method are shown in Fig. 7. The overall trend of the PSD generated by the LPCA–MSSA method matches well with the ground truth trend line. LPCA–MSSA demonstrates the capability to not only suppress the high-frequency noise but also to preserve the primary frequency (~ 0.2) of the signal. Meanwhile, the LPCA-only method fails to perform well in both regard.

Figure 8 shows the sensitivity of the LPCA and LPCA–MSSA methods for 10 repeated CBCT scans in a scatter chart form. Each group contains 10 colored dots where one dot represents the comparison result of the reconstructed waveform versus the ground truth for one scan. Figure 8(a) shows the valley accuracy and peak accuracy and [Fig. 8(b)] shows the phase discrepancy comparison between the reconstructed waveform and the ground truth waveform.

The overall sensitivity of the LPCA–MSSA method is less than 0.2 sec in time accuracy and less than 5% in phase discrepancy. The 95% confidence interval (CI) for the LPCA–MSSA approach was $\pm$ 0.1 sec in time accuracy and $\pm$ 3.4% for overall phase discrepancy. Furthermore, the most distinct difference between the two methods falls in the expiration phase discrepancy, the LPCA-only method has a 95% CI of $\pm$ 9.8 %, and the LPCA–MSSA method has a 95% CI of $\pm$ 0.4%. In general, the respiratory waveforms reconstructed by the LPCA–MSSA method show smaller uncertainties than their counterpart reconstructed by the LPCA-only method with different scans.

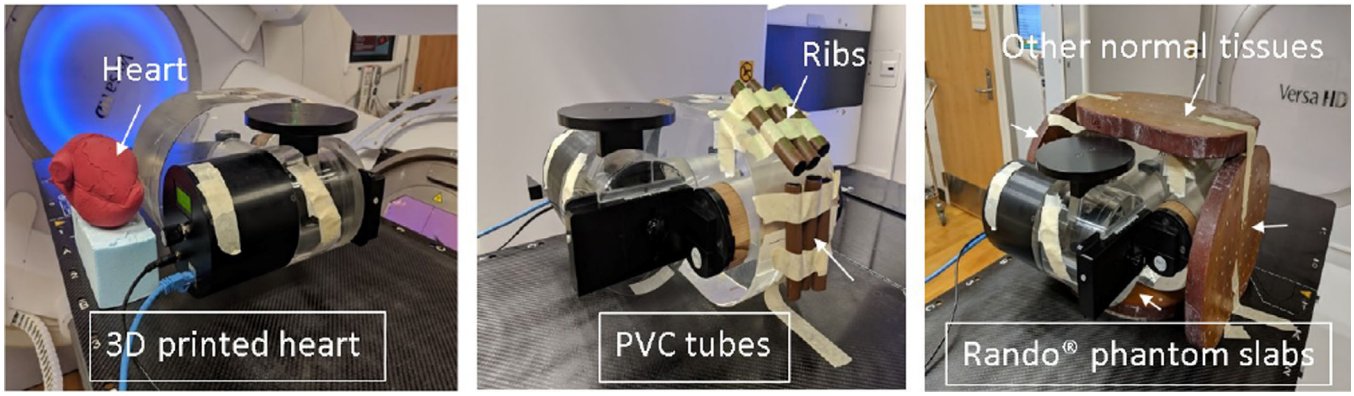

FIG. 5. Simulation of anatomic obstructions, including hearts, ribs, and other normal tissues, on a QUASAR^{TM} respiratory motion phantom.

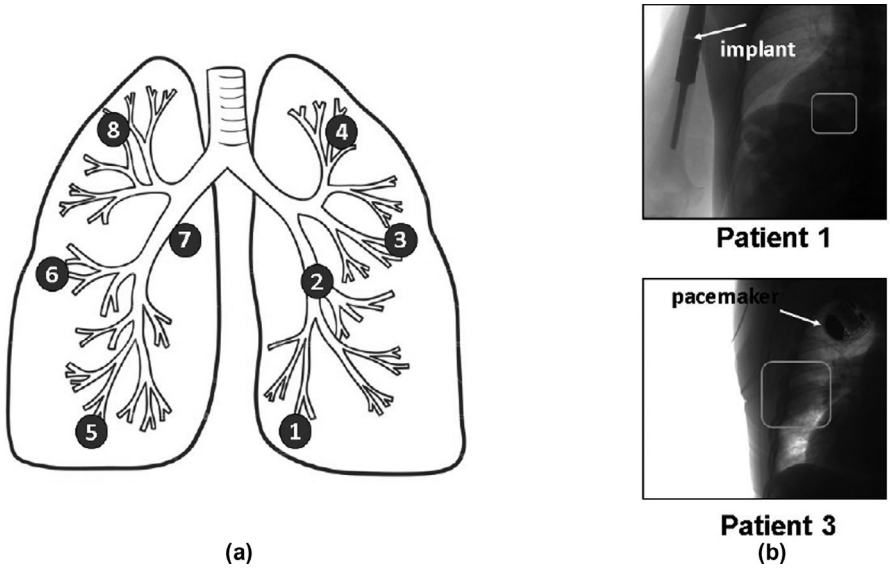

FIG. 6. Clinical lung patient selections. (a) Tumor locations in the lungs of the selected clinical patients from cases 1 through 8. (b) Two patients' cases presenting high-density implants in their bodies. Patient 1 has an arm bone implant. Patient 3 has a pacemaker implant. The boxes indicate regions of tumors.

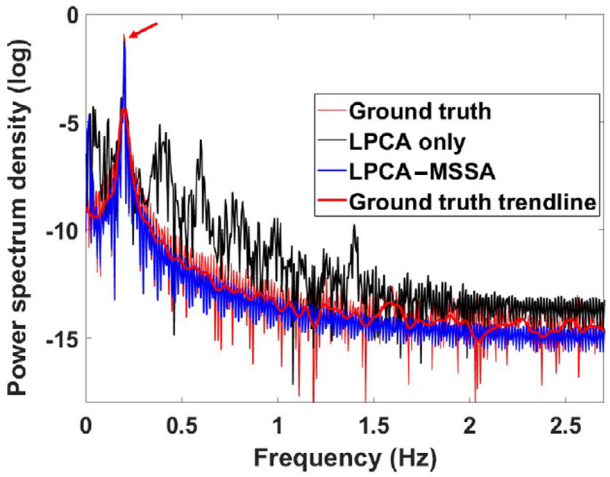

FIG. 7. The results of a sinusoidal respiratory simulation were analyzed using power spectrum density (PSD) in the frequency domain with a logarithmic scale on the vertical axis. The red arrow indicates the peak location that matches the frequency of the original breathing waveform and the rest of the frequencies across the spectrum are induced by the noise of the signal.

Figure 9(a) shows the effect of waveform reconstruction using LPCA–MSSA method on phase-shifting of the external surrogate signal. Figure 9(b) shows the effect using LPCA–MSSA method on arbitrary magnitude variation of external surrogate signal. Under both scenarios, the LPCA–MSSA method performs well for waveform reconstruction whereas waveforms reconstructed by LPCA-only method possess large discrepancy to the ground truth. Among all the scenarios we tested, the overall peak and valley accuracy of reconstructed waveforms by LPCA–MSSA method is -0.009 ± 0.18 sec.

Figure 10 displays the effect of anatomical obstruction on waveform reconstruction using the LPCA–MSSA method. In [Fig. 10(a)], the dash-line framed area is the projection region with most of the obstruction. The performance of the LPCA-only method is deficient in those regions. By contrast, the waveform reconstructed by the LPCA–MSSA method matched the oscillation pattern of the ground truth closely, as shown in [Fig. 10(b)]. The waveform reconstructed by the LPCA–MSSA method has an expiration phase deviation of $1.59 \pm 1.98\%$, a peak accuracy of -0.12 ± 0.28 sec, and a valley accuracy 0.01 ± 0.15 sec, compared with the ground truth for all of the anatomical obstruction scenarios and all of the waveforms we examined.

3.B. Patient study

Table I shows the results for the discrepancy and accuracy of the extracted waveform compared to the reference waveform. For the LPCA–MSSA method, there was an overall phase discrepancy of -1.05 ± 3.0 %, an expiration phase discrepancy of $-1.55 \pm 1.45\%$, a peak accuracy of 0.04 ± 0.13 sec, and a valley accuracy of -0.01 ± 0.15 sec, compared with the reference waveforms. All phase discrepancies were within $\pm$ 5% for all cases, and the peak-valley accuracy was within 0.3 sec. The paired t-test of the phase discrepancy for the LPCA-only and LPCA–MSSA methods gave p-value of 0.0058 and 0.11. Moreover, attempts made to determine the time accuracy for the LPCA-only method were unsuccessful for half of the cases due to noisy waveforms. Therefore, the results are not provided.

Table II shows the variance distribution of each principal component (PC) for all cases. Only the PCs in bold were selected for the final waveform reconstruction. It shows that the first PC for all cases contains more than 80% of the total variance. The total percentage variance used for reconstruction ranges from 89.4 to 98% (two to nine principal components) in the patient study.

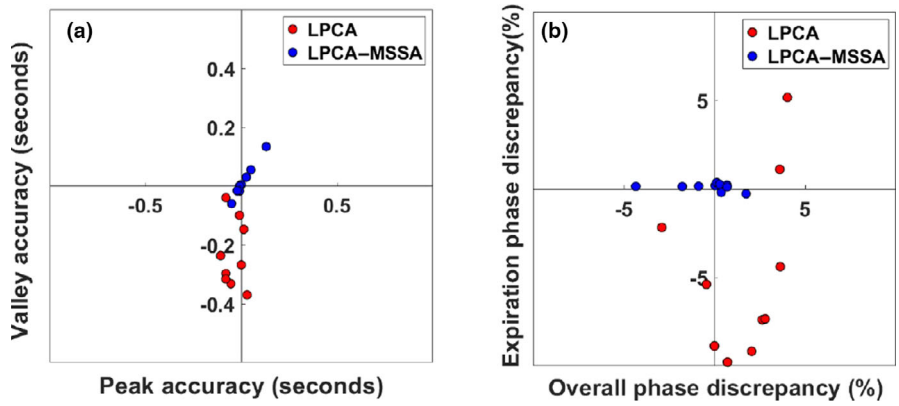

FIG. 8. The sensitivity of the LPCA-only and LPCA–MSSA methods with 10 repeated CBCT scans without any anatomical obstructions. Each circle indicates the discrepancy between the signal extracted from the algorithm and the ground truth for each scan. (a) Peak accuracy versus valley accuracy in seconds (b) Overall phase discrepancy versus expiration phase discrepancy in percentage.

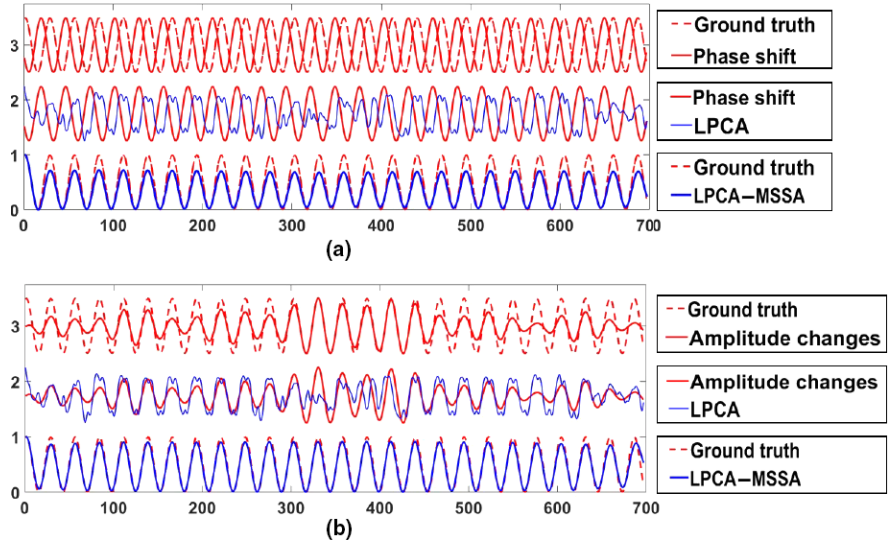

FIG. 9. The assessment of the robustness of the multivariate singular spectrum analysis (MSSA) algorithm. (a) The result of LPCA–MSSA waveform compared to the ground truth (lower panel) while there is a 35% phase shift on the altered external surrogate signal. (b) The result of the LPCA–MSSA waveform compared to the ground truth (lower panel) while there is a gradual amplitude variation on the altered external surrogate signal.

Figure 11 shows the reconstructed waveforms compared with the reference waveforms and their corresponding variance distributions for cases 4 and 6. It illustrates that the LPCA–MSSA approach can accurately recover the respiratory oscillation information by choosing an appropriate percentage variance.

4. DISCUSSIONS

The results suggest that the proposed method is able to reconstruct tumor waveforms with accurate phase information. The accuracy is less than $1/10^{th}$ of phase discrepancy, which is the typical phase sorting requirement. By adding the external surrogate signal into the system, the waveform reconstructed by the LPCA-only method was improved. The MSSA method, which has been widely used in economics,[30] geophysics,[31–34] and other fields, demonstrated its excellent capability of noise removal, oscillation extraction,[35] and time-series (tumor waveforms due to respiration) reconstruction in our study.

In the phantom study, our method shows superior performance compared with the LPCA-only method. A sample case illustrated the perfect match of the trend and peak frequency between the LPCA–MSSA reconstructed waveform and the ground truth in the frequency domain as indicated in Fig. 7. Our method also demonstrates its insensitivity to the timing of the CBCT scan. Since each CBCT acquisition was started arbitrarily, the same angle projection might capture different tumor phase information depending on the patient's respiratory condition during the CBCT scan acquisition. Therefore, the intensity and pattern of the tumor-AS image might vary from scan to scan. This can potentially affect the consistency and precision of the reconstructed waveform. Figure 8 shows the comparison of the reconstruction consistency between

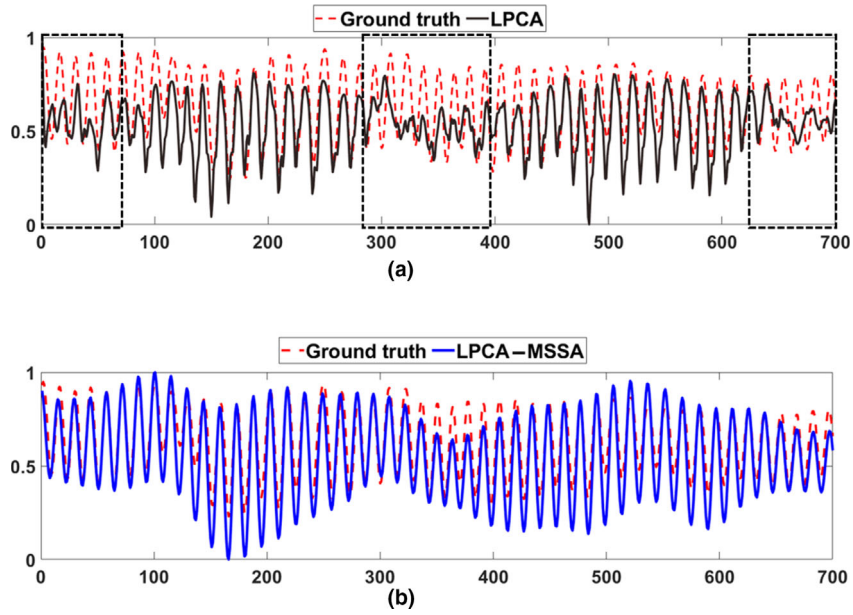

FIG. 10. A cardiac artifact waveform with Rando® phantom slabs. The dashed line indicates the ground truth signal from the optical tracking system. (a) The result of the LPCA-only method compared with the ground truth. The dash-framed regions indicate where the nearly lateral projection angles are. (b) The reconstructed waveform of the LPCA–MSSA method compared with the ground truth.

TABLE I. The phase discrepancy and time accuracy of the extracted respiratory waveform compared with the reference waveform for lung patients. The average breathing period was estimated from the external surrogate waveform. The *P*-value of the paired t-test for the LPCA–MSSA versus the LPCA-only method are listed in the bottom row.

			Average phase discrepancy (%)		Average expiration phase discrepancy (%)		Average peak accuracy (second)	Average valley accuracy (second)
ID	Tumor location	Average period (second)	LPCA–MSSA	LPCA only	LPCA–MSSA	LPCA only	LPCA–MSSA	LPCA–MSSA
1	LLL	2.9	0.84	6.80	−1.25	3.99	−0.03	−0.07
2	LML	3.8	−4.86	1.46	0.38	3.62	0.2	0.2
3	LML	3.8	−1.84	1.31	−4.42	2.73	0.06	−0.1
4	LUL	3.9	4.01	7.14	−2.47	6.54	−0.06	−0.09
5	RLL	3.1	1.59	5.27	−1.23	4.18	−0.05	−0.08
6	RML	3.3	−1.95	−2.35	−1.92	−2.08	0.07	−0.01
7	RML	2.6	−1.96	1.26	−0.3	3.67	0.05	0.04
8	RUL	4.9	−4.2	−3.65	−1.2	−8.62	0.20	0.12
P-value			0.0058		0.11		–	–

Abbreviation: LLL, Left lower lung; LML, left middle lung, LUL, Left upper lung; RLL, right lower lung; RML, right middle lung; RUL, right upper lung; SD, standard deviation.

LPCA-only and our method. The charts demonstrate that our method is much less sensitive to the scan timing than LPCA. The consistency of our method is particularly crucial for the respiratory phase sorting used by 4D-CBCT reconstruction.

Since our approach relies on the external signal for tumor waveform reconstruction, the influence of the external signal quality on the accuracy of the final reconstructed waveform becomes a vital evaluation indicator. Figure 9 suggests that the minimum deterioration effect on the final reconstruction occurs with the proposed method when artificial amplitude variation or phase shift is applied to the original external surrogate signal. It demonstrates the robustness of our method on external surrogate variation. By unique operation of the MSSA method, the correlation between the original and auxiliary signal was built by the covariance matrix. The combined matrix $\mathbb{Y}^{(r)}$ (in Eq. 6) possesses common oscillation features from both signals through the PC selection process. Therefore, the auxiliary signal (external surrogate) is able to enhance the oscillation feature of the original signal without altering its phase or amplitude. Our method is extremely

TABLE II. The variance distribution (%) of the principal component (PC) for each patient. The PCs are listed in descending order based on their eigenvalues. Only the PCs in bold were used for the final respiratory waveform reconstruction, and the sum of the confidence intervals (CI) for those PCs is shown in the last two rows.

		Patient ID							
		1	2	3	4	5	6	7	8
Variance distribution (%)	PC1	**80.74**	**83.86**	**82.34**	**87.85**	**81.70**	**83.06**	**83.35**	**76.56**
	PC2	**11.14**	**5.13**	**2.61**	**3.40**	**5.30**	**5.44**	**4.40**	**3.79**
	PC3	6.34	**4.89**	**2.56**	**3.20**	**4.97**	**5.13**	**4.35**	**3.76**
	PC4	0.95	**0.95**	**1.92**	**0.89**	**1.34**	**1.04**	**3.36**	**2.98**
	PC5	0.34	0.76	1.90	**0.84**	**1.29**	0.90	1.79	**2.51**
	PC6	0.19	0.70	1.07	**0.74**	1.16	0.81	0.74	**2.48**
	PC7	0.1	0.65	0.96	**0.45**	0.60	0.64	0.42	**1.24**
	PC8	0.06	0.63	0.94	**0.35**	0.56	0.39	0.32	**0.96**
	PC9	0.06	0.57	0.43	**0.28**	0.42	0.28	0.32	**0.94**
Number of PCs used		2	4	4	9	5	4	4	9
Confidence interval (%)		**91.9**	**94.8**	**89.4**	**98.0**	**94.6**	**94.7**	**95.5**	**95.2**

Abbreviation: PC, principal component; CI, confidence interval.

beneficial when reconstructing signals with severe disturbance, as shown in Fig. 10. In the figure, the dash-line-framed regions are the regions with severe disturbance in the AS images due to lateral anatomical obstruction. The LPCA-only failed to reconstruct those regions well, whereas our method demonstrated accurate reconstruction capability with the assistance of external surrogate signals. Table I summarizes phase discrepancies between the ground truth and LPCA–MSSA results as well as the phase discrepancies between the ground truth and LPCA-only results. With all four factors listed in the table, LPCA–MSSA results are all superior to the LPCA-only results. Yet, average expiration phase between two methods does not show statistical significance ($P = 0.11$). Thus, we believe more data are needed in the future to demonstrate the superiority of LPCA–MSSA.

Another essential factor that helps our method outperform traditional methods (e.g., LPCA) is the unique AS image generation process. Traditional methods use the whole projection image to generate the AS image in order to enhance the waveform signals. However, these possess some intrinsic drawbacks. Since the projection images include whole lung regions, the generated AS image mixes the phase information of the tumor region with other anatomical regions inside the lung. This causes the true phase information of the tumor itself to be blended into the stronger amplitude signals of the other anatomical regions (e.g., diaphragm). Thus, the phase information of the acquired waveform can be influenced more by those regions than by the tumor itself. Considering the phase difference between the upper lung regions and the diaphragm, the waveform reconstructed using whole projections could have some innate phase discrepancy compared to the real tumor phase, depending on the location of the tumor. By contrast, our method uses only the cropped tumor region to generate the tumor-AS image, so the nontumor disturbances are disregarded and the tumor-only phase information is acquired. The signal enhancement is eventually produced by the MSSA algorithm with the assistance of the external surrogate signals.

In the patient study, different strategies for CI threshold selection were tested to model an optimal clinical environment. A scoring system was developed for the CI threshold value selection. The threshold values were chosen on a case-by-case basis and determined by the irregularity of the initial LPCA waveform (category 1) and the degree of anatomic obstruction (category 2) for each CBCT scan. More specifically, if the initial LPCA waveform presented irregularities (when any of the breathing cycle lengths possessed more than 1 sec variation compared to the median breathing cycle length), the scan was scored as 1 in category 1, and 0 otherwise; if the tumor was situated in the upper lung, the scan was scored as 1 in category 2 because it contained severe shoulder obstruction on the lateral projection views, and 0 otherwise. The final score was obtained by summing the scores for these two categories. Finally, the CI threshold was set at various levels according to the final score for each case: 0.9 (total score = 0), 0.95 (total score = 1), or 0.98 (total score = 2). As shown in Table II, patient case No. 4 is an upper lung case (category 2, score = 1) with irregular breathing pattern (category 1, score = 1); it required the CI to be equal to or greater than 98%. With this scoring system, all cases presented in our study achieved excellent waveform reconstruction accuracy. A balance between the number of components used and the accuracy of the reconstructed phase information was conducted subjectively. A more robust and systematic strategy needs to be developed in the future.

In this study, an OTS reflective marker was used as a respiratory oscillation indicator for continuous monitoring during the treatment. Moreover, the external surrogate signal can be any distinct oscillation signal related to the patient respiratory motion, such as external surface signals[36] or internal ultrasound tracking signals.[37] These can all be used to assist tumor phase recognition by applying the proposed algorithm

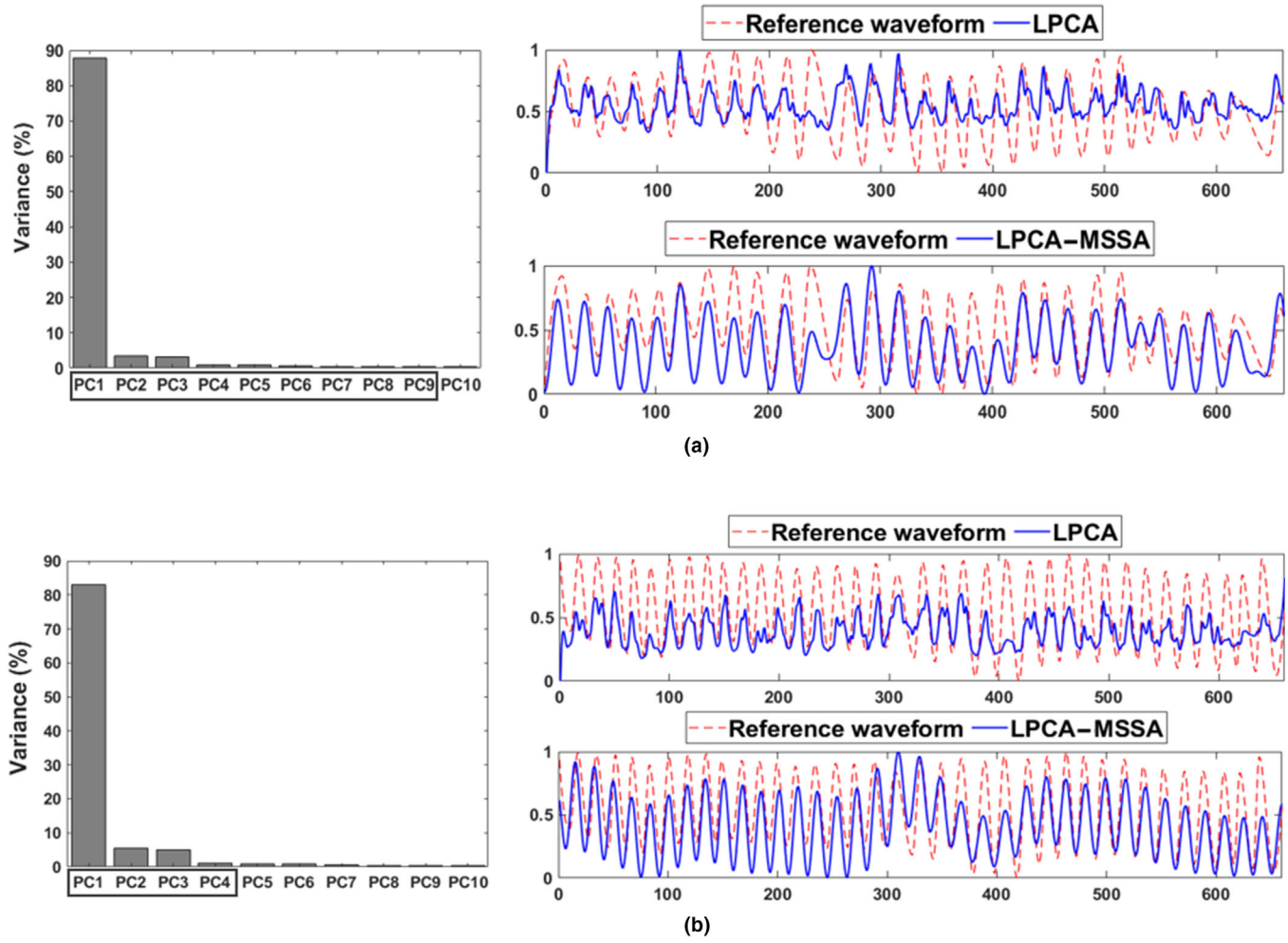

FIG. 11. The reconstructed waveform compared to the reference waveform with the variance percentage (%) of each principal component (PC) displayed in a bar chart. (a) Patient ID 4: PC1 to PC9 were used for LPCA–MSSA reconstruction. (b) Patient ID 6: PC1 to PC4 were used for LPCA–MSSA reconstruction. The right upper panel displays the LPCA-only waveform compared with the reference waveform; the right lower panel displays the LPCA–MSSA waveform compared with the reference waveform.

to future clinical implementation. For example, the phase sorting method can be utilized for 4D-CBCT phase sorting. To further utilize the existing correlation from the covariance, our algorithm could be used as a model-free based approach to reconstruct the respiratory phase information in real time. The MSSA can feed in the multiple channels that are greater than 2, and has the ability to predict the dynamics of the respiratory phenomena. For future clinical applications, it can be used for determination of gating threshold for gating-based treatment.

One limitation of our study is that the current technique was only tested on ELEKTA CBCT acquisition settings. Thus, further investigation with other commercial linac accelerator systems or technology needs to be performed to assess the robustness of our method in future.

5. CONCLUSIONS

The LPCA–MSSA algorithm is capable of extracting tumor phase information at all imaging angles. With the aid of the oscillation information of the external surrogate, and accompanying information of the preliminary internal tumor signal, the prediction accuracy was improved as compared to the LPCA-only algorithm. Most importantly, with sufficient accuracy, it enables us to use it as the ground truth for 4D-CBCT reconstruction, respiratory gating treatment, and other clinic implementations that require accurate tumor phase information.

ACKNOWLEDGMENTS

We thank Dr. Hao Yan from OUR United Corporation, China, for discussions on his original work.

CONFLICT OF INTEREST

The authors have no conflict of interest to declare.

[a)]Author to whom correspondence should be addressed. E-mail: lubo@shands.ufl.edu; Telephone: 352-265-8217; FAX: 352-265-0759

REFERENCES

1. Keall PJ, Mageras GS, Balter JM et al The management of respiratory motion in radiation oncology report of AAPM task group 76 AAPM report 91. *Med Phys*. 2006;33:3874–3900.
2. Korreman SS. Image-guided radiotherapy and motion management in lung cancer. *Brit J Radiol*. 2015;88:20150100.
3. Giraud P, Garcia R. Respiratory gating for radiotherapy: main technical aspects and clinical benefits. *B Cancer*. 2010;97:847–856.
4. Kurup G. CyberKnife: a new paradigm in radiotherapy. *J Med Phys*. 2010;35:63–64.
5. Cui Y, Dy JG, Sharp GC, Alexander B, Jiang SB. Robust fluoroscopic respiratory gating for lung cancer radiotherapy without implanted fiducial markers. *Phys Med Biol*. 2007;52:741–755.
6. Willoughby TR, Forbes AR, Buchholz D et al Evaluation of an infrared camera and X-ray system using implanted fiducials in patients with lung tumors for gated radiation therapy. *Int J Radiat Oncol*. 2006;66:568–575.
7. Berbeco RI, Mostafavi H, Sharp GC, Jiang SB. Towards fluoroscopic respiratory gating for lung tumours without radiopaque markers. *Phys Med Biol*. 2005;50:4481–4490.
8. Ozhasoglu C, Murphy MJ. Issues in respiratory motion compensation during external-beam radiotherapy. *Int J Radiat Oncol*. 2002;52:1389–1399.
9. Yan H, Wang XY, Yin WT et al Extracting respiratory signals from thoracic cone beam CT projections. *Phys Med Biol*. 2013;58:1447–1464.
10. Chao M, Wei J, Li TF, Yuan YD, Rosenzweig KE, Lo YC. Robust breathing signal extraction from cone beam CT projections based on adaptive and global optimization techniques. *Phys Med Biol*. 2016;61:3109–3126.
11. Lee D, Greer PB, Paganelli C, Ludbrook JJ, Kim T, Keall P. Audiovisual biofeedback improves the correlation between internal/external surrogate motion and lung tumor motion. *Med Phys*. 2018;45:1009–1017.
12. Mittauer K, Paliwal B, Hill P et al A new era of image guidance with magnetic resonance-guided radiation therapy for abdominal and thoracic malignancies. *Cureus*. 2018;10:e2422.
13. Menten MJ, Wetscherek A, Fast MF. MRI-guided lung SBRT: Present and future developments. *Phys Medica*. 2017;44:139–149.
14. Seiler PG, Blattmann H, Kirsch S, Muench RK, Schilling C. A novel tracking technique for the continuous precise measurement of tumour positions in conformal radiotherapy. *Phys Med Biol*. 2000;45:N103–N110.
15. Sharp GC, Jiang SB, Shimizu S, Shirato H. Prediction of respiratory tumour motion for real-time image-guided radiotherapy. *Phys Med Biol*. 2004;49:425–440.
16. Tang XL, Sharp GC, Jiang SB. Fluoroscopic tracking of multiple implanted fiducial markers using multiple object tracking. *Phys Med Biol*. 2007;52:4081–4098.
17. Ohta K, Shimohira M, Iwata H et al Percutaneous fiducial marker placement under CT fluoroscopic guidance for stereotactic body radiotherapy of the lung: an initial experience. *J Radiat Res*. 2013;54:957–961.
18. Willoughby TR, Kupelian PA, Pouliot J et al Target localization and real-time tracking using the calypso 4D localization system in patients with localized prostate cancer. *Int J Radiat Oncol*. 2006;65:528–534.
19. Kupelian P, Willoughby T, Mahadevan A et al Multi-institutional clinical experience with the Calypso System in localization and continuous, real-time monitoring of the prostate gland during external radiotherapy. *Int J Radiat Oncol*. 2007;67:1088–1098.
20. Booth J, Booth J, Hardcastle N et al First clinical implementation of electromagnetic transponder-guided MLC tracking for lung stereotactic ablative radiation therapy. *Int J Radiat Oncol*. 2016;96:S47.
21. Kothary N, Heit JJ, Louie JD et al Safety and efficacy of percutaneous fiducial marker implantation for image-guided radiation therapy. *J Vasc Interv Radiol*. 2009;20:235–239.
22. Bhagat N, Fidelman N, Durack JC et al Complications associated with the percutaneous insertion of fiducial markers in the thorax. *Cardiovasc Inter Rad*. 2010;33:1186–1191.
23. Trumm CG, Haussbler SM, Muacevic A et al CT fluoroscopy-guided percutaneous Fiducial marker placement for Cyberknife stereotactic radiosurgery: technical results and complications in 222 consecutive procedures. *J Vasc Interv Radiol*. 2014;25:760–768.
24. Nelson C, Starkschall G, Balter P, Morice RC, Stevens CW, Chang JY. Assessment of lung tumor motion and setup uncertainties using implanted fiducials. *Int J Radiat Oncol*. 2007;67:915–923.
25. Hong JC, Eclov NCW, Yu Y et al Migration of implanted markers for image-guided lung tumor stereotactic ablative radiotherapy. *J Appl Clin Med Phys*. 2013;14:77–89.
26. Zijp L, Sonke J-J, van Herk Mv M. Extraction of the respiratory signal from sequential thorax Cone-Beam X-ray images. Paper presented at: Proceedings of the 14th ICCR2004; Seoul, Korea.
27. Kavanagh A, Evans PM, Hansen VN, Webb S. Obtaining breathing patterns from any sequential thoracic x-ray image set. *Phys Med Biol*. 2009;54:4879–4888.
28. Vergalasova I, Cai J, Giles W, Segars WP, Yin FF. Evaluation of the effect of respiratory and anatomical variables on a Fourier technique for markerless, self-sorted 4D-CBCT. *Phys Med Biol*. 2013;58:7239–7259.
29. Golyandina N, Nekrutkin V, Zhigljavsky AA. *Analysis of Time Series Structure: SSA and Related Techniques*. Chapman and Hall/CRC. 2001.
30. Hassani H, Zhigljavsky A. Singular spectrum analysis: methodology and application to economics data. *J Syst Sci Complexity.* 2009;22:372–394.
31. Serita A, Hattori K, Yoshino C, Hayakawa M, Isezaki N. Principal component analysis and singular spectrum analysis of ULF geomagnetic data associated with earthquakes. *Nat Hazards Earth Syst Sci*. 2005;5:685–689.
32. Bozzo E, Carniel R, Fasino D. Relationship between Singular spectrum analysis and Fourier analysis: theory and application to the monitoring of volcanic activity. *Comput Math Appl*. 2010;60:812–820.
33. Ghil M, Allen MR, Dettinger MD et al Advanced spectral methods for climatic time series. *Rev Geophys*. 2002;40.
34. Vautard R, Ghil M. Singular spectrum analysis in nonlinear dynamics, with applications to paleoclimatic time-series. *Physica D*. 1989;35:395–424.
35. Groth A, Ghil M. Monte Carlo singular spectrum analysis (SSA) revisited: detecting oscillator clusters in multivariate datasets. *J Climate*. 2015;28:7873–7893.
36. Schoffel PJ, Harms W, Sroka-Perez G, Schlegel W, Karger CP. Accuracy of a commercial optical 3D surface imaging system for realignment of patients for radiotherapy of the thorax. *Phys Med Biol*. 2007;52:3949–3963.
37. Mostafaei F, Tai A, Gore E et al Feasibility of real-time lung tumor motion monitoring using intrafractional ultrasound and kV cone beam projection images. *Med Phys*. 2018;45:4619–4626.